# Synthesis of submicrometric dendritic iron particles in an Electrochemical and Vibrating Hele-Shaw cell: study of the growth of ramified branches

A. Iranzo, F. Chauvet*, T. Tzedakis*

*Laboratoire de Génie Chimique, Université de Toulouse, CNRS-INPT-UPS, Toulouse, France*

*Keywords:*
iron electrodeposition
sonoelectrochemistry
ramified growth
nucleation
microstreaming

A B S T R A C T

The purpose of this study is to explore a new synthesis way for the production of iron nanoparticles exploiting the nanometric structure of long ramified iron branches formed by electrodeposition in a Hele-Shaw cell. After the growth, these branches are fragmented by the action of a vibrating element (piezoelectric disk) integrated into the cell. The emphasis is put on the growth of the ramified iron branches which is performed by galvanostatic electrodeposition in a stagnant electrolyte ($FeCl_2$) inside the Hele-Shaw cell (50 μm deep). The competition between the co-formation of $H_2$ bubbles ($H^+$ reduction) and the growth of ramified iron branches ($Fe^{II}$ reduction) is analyzed by varying both the applied current density $j$ and the $FeCl_2$ concentration. Two regimes, depending mainly on $j$, are highlighted: below a threshold current density of 8 mA/cm$^2$ only $H_2$ bubbles are formed, while above this threshold, iron branches grow accompanied by the formation of $H_2$ bubbles which nucleate and grow at the top of the branches during their formation. The $H_2$ bubbles influence the branches growth especially at low $j$ (<24 mA/cm$^2$) when the growth velocity of the branches is low compared to the growth rate of the bubbles. At higher $j$ (>24 mA/cm$^2$), the branches follow a columnar growth with a constant front velocity, well predicted by the theory. Scanning Electron Microscopy (SEM) of the iron branches shows a dendritic structure constituted of nanometric crystallites, whose size depends on the local growth velocity: increasing the growth velocity from 3.6 μm/s to 40 μm/s leads to a decrease in the crystallites size, from ~1 μm to ~10 nm. Using the acoustic vibrations (4 kHz) of the piezoelectric disk, these fragile branches are successfully fragmented into submicrometric fragments of dendrites exhibiting high specific surfaces S/V (equivalent to the S/V of nanoparticles of 30 nm diameter). Advantages/Drawbacks compared to other synthesis ways as well as the optimization of the proposed synthesis are discussed.

## 1. Introduction

Metallic iron nanoparticles attract significant interest both for their magnetic and catalytic properties in various fields (medical, energy, and environment). In the medical field, even if iron oxide nanoparticles have been investigated for their magnetic properties, for Magnetic Resonance Imaging (MRI) [1] or cancer treatment [2], they appear to be less efficient when compared to iron nanoparticles which exhibit enhanced magnetic properties [3]. In addition, iron nanoparticles are increasingly investigated in the treatment of contaminated waters and soils [4–6] due to their reductive properties. Indeed, due to the low standard electrode potential of the $Fe^{2+}/Fe^0$ system ($E^\circ = -0.44$ V/SHE), their high specific surface and their porous iron oxide/hydroxide outside layer, these iron nanoparticles show a high reactivity and allow the removal of pollutants [5] such as ions of heavy metals or chlorinated organic compounds [7].

Conceptually, nanoparticles can be synthesized through two global approaches, top-down and bottom-up. The first one consists of using a large-sized material (micrometric particles for examples) which is chemically or physically cut off until the nanometric size is reached. The bottom-up approach consists of the reverse process; small building blocks (like atoms) are assembled to form nanoparticles. Based on these two global approaches, various physical or chemical syntheses have been explored to produce iron nanoparticles (ball-milling [8], thermal reduction of iron salt [9,10], iron salt wet-chemical reduction [11,12]).

* Corresponding author
*E-mail addresses:* chauvet@chimie.ups-tlse.fr (F. Chauvet), tzedakis@chimie.ups-tlse.fr (T. Tzedakis).

Among the wet-chemical syntheses, the production of iron nanoparticles by reduction of an iron salt by a borohydride salt (colloidal synthesis) is a method commonly employed at the laboratory scale [7]. Nevertheless, this synthesis requires specific conditions, first because of the risk of gaseous hydrogen production (caused by borohydride oxidation) and secondly due to the toxicity, corrosiveness, and flammability of the borohydride reductant [9,13]. Additionally, a step of purification is required to separate the produced nanoparticles from the remaining reacting species and byproducts (dialysis, ion exchange resin, centrifugal or filtration processes). This is required for several reasons: enhancement of the colloidal stability, to avoid the presence of salt crystals during dry characterization of the particles and to avoid contamination/pollution effects by residues of the synthesis in the final application.

Another technique to produce metallic nanoparticles, here called "sonoelectrochemical synthesis", combines electrochemical and ultrasonication processes. It consists in the electrodeposition of iron nanoparticles (nuclei) on a cathode surface which is subjected to power ultrasound (20 kHz). The propagation of the ultrasonic waves induces cavitation bubbles which, during their violent collapses, create strong enough fluid motion to detach the iron nanoparticles from the electrode surface (Fig. 1a)). Both processes, electrodeposition and ultrasound, can be applied either simultaneously [14] or sequentially [15]. This technique appears to be a promising alternative, avoiding the use of a reductive chemical agent, but: i) the purification step is, here again, required (removal of the supporting electrolyte and remaining metallic precursor) and ii) the ultrasound process suffers from a low energetic yield (a large part of the mechanical energy is consumed by the cavitation and streaming generated far from the electrode surface, and so useless for the deposit dispersion).

On the basis of this last technique, we propose to explore in the present paper a new synthesis route aiming to be cost effective, safe and implying a limited number of steps. As in the case of the sonoelectrochemical synthesis, it consists in producing electrochemically the metallic iron particles but, instead of limiting the iron growth to obtain nuclei lying on the electrode surface, the electrodeposition is driven for longer times giving rise to "long" ramified iron branches which are then fragmented via acoustic vibrations, Fig. 1b).

To that end, an "Electrochemical and Vibrating Hele-Shaw cell" has been designed. It consists of a Hele-Shaw cell (a thin gap cell, 50 μm deep) integrating a low-frequency acoustic device (piezoelectric disk, PZT, resonance frequency = 4 kHz) to induce the vibrations (Fig. 2).

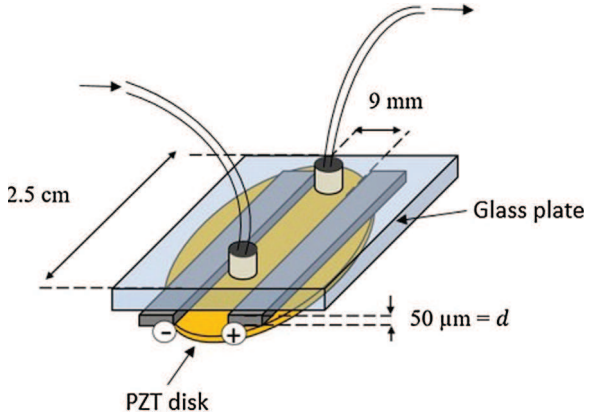


**Fig. 2.** Schematic representation of the Electrochemical and vibrating Hele-Shaw cell used in this study.

The use of such a confined geometry allows the control of the iron growth and the generation of ramified deposits. When a current is applied to the cell, the metallic cations $M^{z+}$ are reduced into metal $M^0$ inducing the decrease of the $M^{z+}$ concentration at the cathode interface (no fluid circulation into the cell). When the interfacial $M^{z+}$ concentration reaches zero, the metal has to grow under the form of a porous deposit (ramified branches) through a succession of nucleation/growth events (or the water reduction takes place) for the current to keep flowing through the cell [16]. Depending on the operating parameters (applied current or cell voltage and precursor concentration), the resulting ramified deposits exhibit one of the three main morphologies (arrangement of the branches): fractal, columnar and dendritic [17,18]. The branches are known to be constituted of small crystallites which could be nanometric (as shown in the case of the formation of ramified copper branches [19]). Thus, the idea, proposed in this work, is to exploit the small granular structure of the branches, for the case of an iron deposit, to produce a suspension of iron nanoparticles via the fragmentation of branches induced by the PZT vibrations. The size of the crystallites that constitute the iron branches being dependent on the applied current density [19], this synthesis route offers an external control of the produced nanoparticles, at least in term of size, via the operating parameters (applied current and iron precursor concentration). Additionally, in

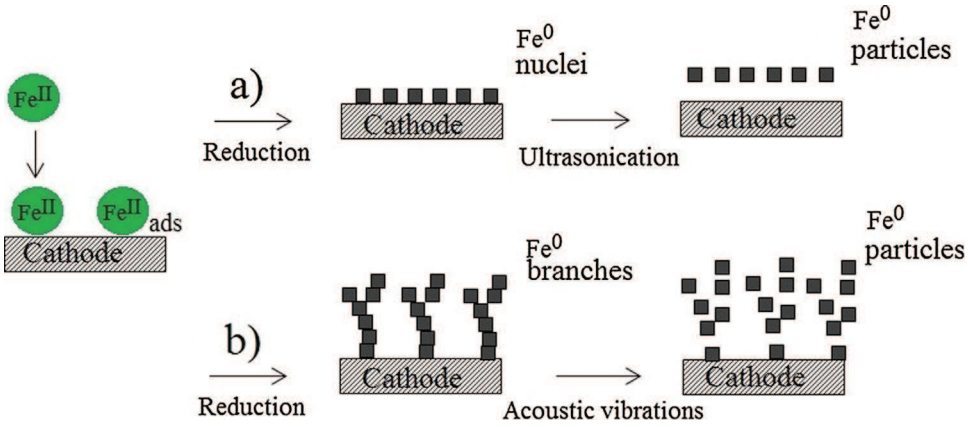


**Fig. 1.** Schematic representation of: a) the classical sonoelectrosynthesis which is the removal by ultrasound of iron nanoparticles electrodeposited on an electrode substrate, b) the new synthesis proposed in this study which consists of the fragmentation under acoustic vibrations of ramified iron electrodeposits.

contrast with the sonoelectrochemical synthesis, the integration of the PZT to the Hele-Shaw cell allows localizing and concentrating the mechanical action on the metallic crystallites assemblies. Last but not the least, in this microfluidic-like device, the branches could be rinsed before their fragmentation, which should avoid the final purification step.

As indicated in a previous work [20] and also in [21], on an iron electrode, the reduction of $Fe^{II}$ ($FeCl_2$, $(NH_4)_2Fe(SO_4)_2$ and $FeSO_4$ for $pH < \sim 4$) into $Fe^0$ is accompanied by the reduction of free protons $H^+$. Therefore, hydrogen bubbles formation is expected during the electrodeposition experiments in the Hele-Shaw cell (as shown in S. Bodea et al. [22]). This issue is specifically studied in the following.

The integration of the low-frequency acoustic device in the Hele-Shaw cell is inspired by its use in microfluidic chips to enhance mixing [23–25]. In these works, it has been established that the presence of bubbles, trapped into specially designed microchannels, is needed to allow an efficient mixing [23]. The vibration of the PZT induces the oscillation of the bubbles that generates microstreaming (a stationary and asymmetric fluid flow around the bubbles [26]). We propose here to take advantage of the microstreaming generated by the co-produced $H_2$ bubbles for the fragmentation of the branches.

This study focuses on the effect of both the $FeCl_2$ concentration and the applied current density on i) the growth of ramified iron branches in the Hele-Shaw cell and ii) the influence of the co-

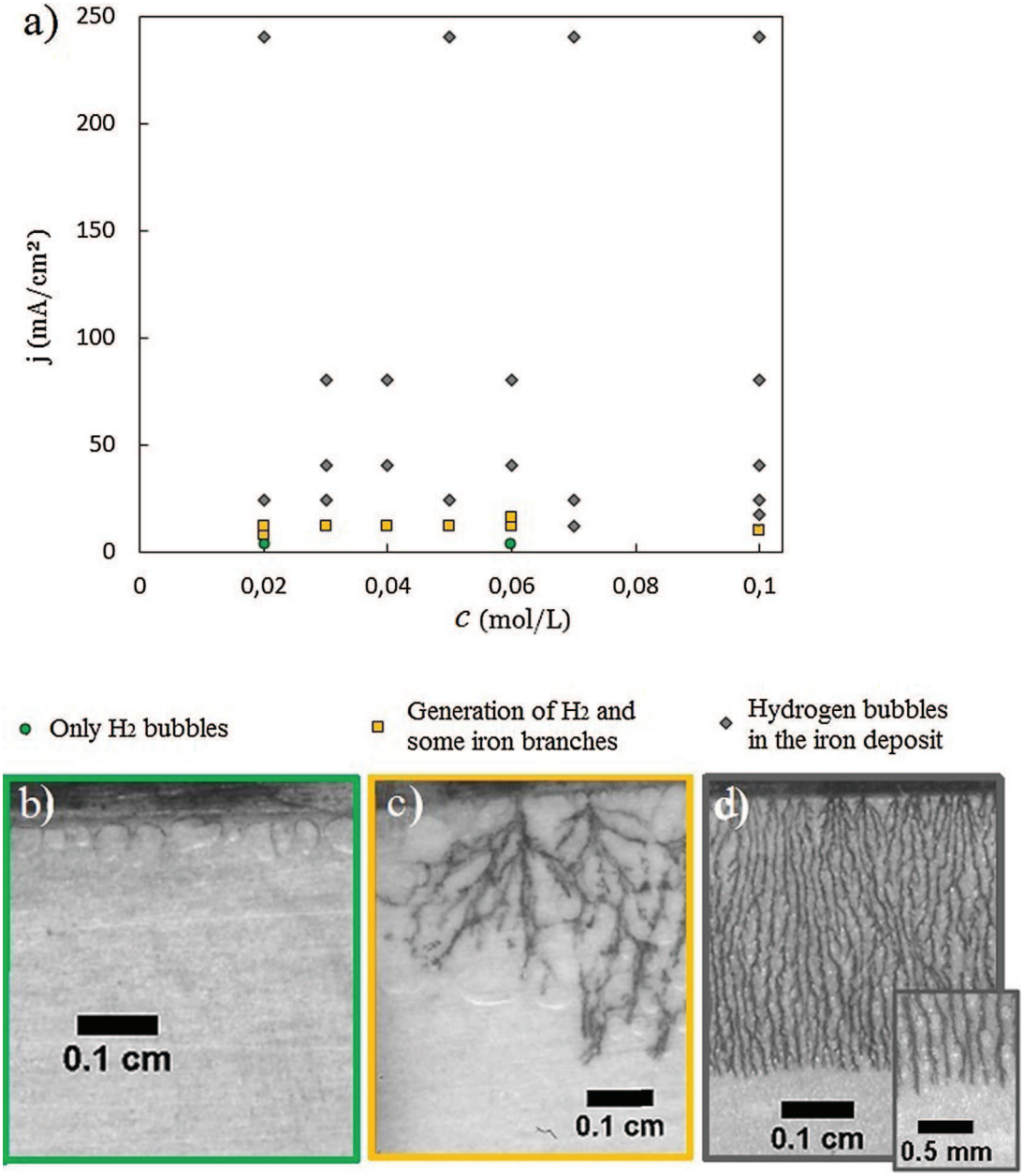


**Fig. 3.** Synthetic results of various electrolyses carried out at various current densities and for various concentrations of the iron precursor ($FeCl_2$) without supporting electrolyte. For each $FeCl_2$ concentration, different current densities are applied, and the phenomena occurring in the Hele-Shaw cell are shown in a); green circles: only $H_2$ bubbles, yellow squares: mainly $H_2$ bubbles with some iron branches, grey diamonds: $H_2$ bubbles and iron branches which fill the space uniformly. For each case, an image of a typical deposit, obtained under the corresponding conditions, is shown in b) 0.02 M, 4 mA/cm$^2$, c) 0.06 M, 12 mA/cm$^2$ and d) 0.1 M, 80 mA/cm$^2$. (For interpretation of the references to colour in this figure legend, the reader is referred to the web version of this article.)

produced $H_2$ bubbles. SEM and Transmission Electron Microscopy (TEM) are used to observe respectively the structure of the branches as well as the particles resulting from the iron branches fragmentation (the fragmentation mechanism will be detailed in another paper). The purity of the obtained aqueous suspension of iron particles, in term of electrolyte salt content (i.e. mass fraction of the metallic iron), is determined and the result is compared to the one obtained with the colloidal and the sonoelectrochemical syntheses.

## 2. Experimental

### 2.1. Chemicals

Iron (II) salt solutions are prepared using normapur solid $FeCl_2$ (Sigma-Aldrich) in ultrapure water (18.2 MΩ.cm); no supporting electrolyte is used. The natural pH of the $FeCl_2$ solutions varies from 3.9 to 3.3 depending on the $FeCl_2$ concentrations used (from 0.02 to 0.1 M respectively). The presence of dissolved $O_2$ must be avoided to prevent its co-reduction during the electrodeposition and to limit the $Fe^0$ corrosion. All the solutions are deaerated (Argon, 1 bar), during 15 min (∼30 mL) before being collected by a gastight syringe (Hamilton 1 mL, 1001LT) and injected into the Hele-Shaw cell.

### 2.2. Experimental set-up and methods

The Hele-Shaw cell is constituted of two iron plates (the electrodes) of a thickness of 50 μm (purity ≥ 99.5%), which are 9 mm apart and sandwiched between a glass plate and the PZT (ABT-441-RC, Radiospare). The length of the electroactive zone is 2.5 cm, Fig. 2.

The face of the glass plate exposed to the channel is entirely covered by transparent laboratory parafilm sheet acting as a gasket to avoid leakages while the surface of the PZT is covered by an adhesive tape ensuring its protection against corrosion. The contours of the Hele-Shaw cell are closed by applying an adhesive paste. Two clamps, pressing on the glass plates, are used to hold the assembly. The cell is filled with the ferrous ion solution using the gastight syringe via two microtubes (PTFE) connected to the cell by fluidic connections made by drilling holes in the glass plate and by gluing Nanoport connectors (Idex-hs) on them. Special care is taken to avoid the introduction of atmospheric oxygen inside the channel. The cell is maintained horizontally to avoid natural convection which could influence the branches growth and so their structure [27,28]. The cell can easily be dismantled to be cleaned, or to recover the iron deposits for SEM observations. The electrodes are manually polished using a paper grid (P1200) to operate with a reproducible state of the surface of the electrodes. The electrolyses are performed with a potentiostat (Autolab PGSTAT100N). Experiments are carried out at room temperature ($18 < T(°C) < 22$).

A typical experiment consists in filling the cell with the electrolyte, then a constant current is applied between the electrodes and the growth of the iron branches, on the cathode, is visualized by a camera. The oxidation of the iron made anode prevents the production of both $O_2$ (bubbles never observed) and $Fe^{III}$. After their formation, the metallic branches are rinsed by a flow of deaerated ultrapure water using a syringe pump. A sufficiently low flow rate, ∼100 μL/min, is applied to avoid both damaging the iron branches and the removal of the hydrogen bubbles. Besides, no change in the bubbles size is observed, due to both the low solubility (∼0.8 mM) of $H_2$ in water and also due to the low surface area of the liquid gas interfaces of the crushed bubbles in this confined geometry (the smallest apparent diameter of bubbles being equal to 100 μm). The PZT is then activated during ∼15 s to fragment the branches. The fragmented particles are collected by pushing them through the cell applying a flow of deaerated ultrapure water.

### 2.3. Observations of the obtained iron electrodeposits

#### 2.3.1. Optical observation of the growth of the ramified iron branches

The growth of the ramified iron branches is observed by reflection using a fiber optic illuminator and a camera PCO pixelfly connected with a 105 mm macro lens (field of view ≈ 5 mm × 5 mm). A picture of the deposit is taken every 5 seconds to monitor the evolution of its growth.

#### 2.3.2. SEM observation of the ramified iron branches and preparation of the samples

To observe the structure of the obtained deposit, SEM pictures of the ramified iron branches are taken. The iron deposits are fragile, and the recovery of the ramified structure requires special caution. After the rinsing phase, the cell is opened which induces strong modifications of the branches pattern, but without damaging the microstructure. The deposit is recovered on an adhesive carbon tape and dried under atmospheric conditions. The structure of the iron branches (before fragmentation) is observed by SEM with a JEOL JSM 7100F TTLS or a JEOL JSM 7800F Prime-EDS.

#### 2.3.3. TEM observation of the particles suspension and preparation of the samples

A drop of the suspension, containing the fragmented particles, is left to dry on a TEM grid before analysis with JEOL JSM 2100F-EDS.

## 3. Results and discussion

### 3.1. Growth of ramified iron branches accompanied with the formation of $H_2$ bubbles in the Hele-Shaw cell

To determine the conditions allowing the growth of the iron branches, in the Hele-Shaw cell used, several galvanostatic electrolyses are performed using a stagnant $FeCl_2$ solution, by varying the concentration $c$, from 0.02 M to 0.1 M (the natural pH varying from 3.9 to 3.3) and the applied current density from 4 to 240 mA/cm$^2$ (relative to the initial geometrical surface of the electrode). The obtained results can be classified into three different groups (see Fig. 3), depending mainly on the current density $j$ and remarkably independently of the concentration (in the examined range):

- $j < \sim 8$ mA/cm$^2$: $H_2$ bubbles are produced, and no iron branches are observed (green circles in Fig. 3a) and Fig. 3b))
- $\sim 8 < j$ (mA/cm$^2$) $< \sim 16$: large $H_2$ bubbles are produced, and some partially broken ramified iron branches are observed (yellow squares in Fig. 3a) and Fig. 3c))
- $j > \sim 16$ mA/cm$^2$: small $H_2$ bubbles nucleate and grow at the top of the iron branches, and they are continuously left behind the moving front (gray diamonds in Fig. 3a) and Fig. 3d)).

These results, in agreement with those of Heresanu [29], highlight that there is a threshold current density (≈8 mA/cm$^2$ here, mainly devoted to the $H^+$ reduction) to overcome in order to produce iron branches.

For an applied current density $j < 8$ mA/cm$^2$, the initial potential is not sufficiently cathodic to start the reduction of $Fe^{II}$. Due to the decrease in the interfacial concentration of $H^+$, the potential of the cathode decreases until it reaches the potential enabling to induce the reduction of the $Fe^{II}$ ions. An additional time is then required to achieve the growth of the ramified deposit, which corresponds to

the time necessary to fully deplete the $Fe^{II}$ at the cathode surface [30]. The experimental results suggest that this last condition is never obtained for $j < 8\ mA/cm^2$.

For an applied current density $j > 8\ mA/cm^2$, the initial potential is sufficiently cathodic to induce the simultaneous reduction of $Fe^{II}$ and $H^+$. Due to both the high value of the current and the low concentration of $H^+$ (compared to $Fe^{II}$ concentration), the fraction of the current used for the $H^+$ reduction is low compared to the one used for the $Fe^{II}$ reduction. This shortens the depletion time for the $Fe^{II}$ and makes the growth of iron branches possible, as observed in the experiments when applied current densities $>8\ mA/cm^2$. A model based on the coupling between the transient semi-infinite diffusion profiles of $H^+$ and $Fe^{II}$ with Butler-Volmer equations will be provided in another paper.

However, the transition between these two limiting cases is not easy to model since the growth of $H_2$ bubbles at the cathode surface can change the electrolysis conditions locally:

- $H_2$ bubbles cover the electroactive surface of the cathode implying the increase of the current density imposed to the free surface, and then, could favor the start of a branch growth.
- $H_2$ bubbles can also totally isolate some of the iron branches from the solution and consequently block their growth.

Both cases are respectively highlighted in Fig. 4a) and b).

Even if $H_2$ bubbles are produced whatever the operating conditions, the deposit growth appears to be less affected by their presence at high current density (for $j > 16\ mA/cm^2$). This is because, for these conditions, the growth velocity of the branches is higher than the bubbles growth rate, leading to the formation of smaller bubbles, less disruptive than those produced at lower current density.

### 3.2. Morphologies of the iron electrodeposits in the Hele-Shaw cell

The morphologies of the obtained iron electrodeposits, at the macroscopic scale (arrangement of the branches), are reported in Fig. 5 as a function of the applied current density and the precursor concentration. The objective here is to examine the effect of the $H_2$ bubbles, electro-generated simultaneously with the iron deposition, on the morphology transitions and to compare with the main deposits patterns, and the associated transitions, usually observed in absence of bubbles (fractal-columnar-dendritic) [17,18].

Two main morphologies are distinguished in Fig. 5: the fractal and the columnar; no dendritic morphologies are observed at this macroscopic scale (field of view $\approx 5\ mm \times 5\ mm$).

Even if it is not visible in Fig. 5 (especially at the higher current densities), the formation of bubbles, during the growth of the iron

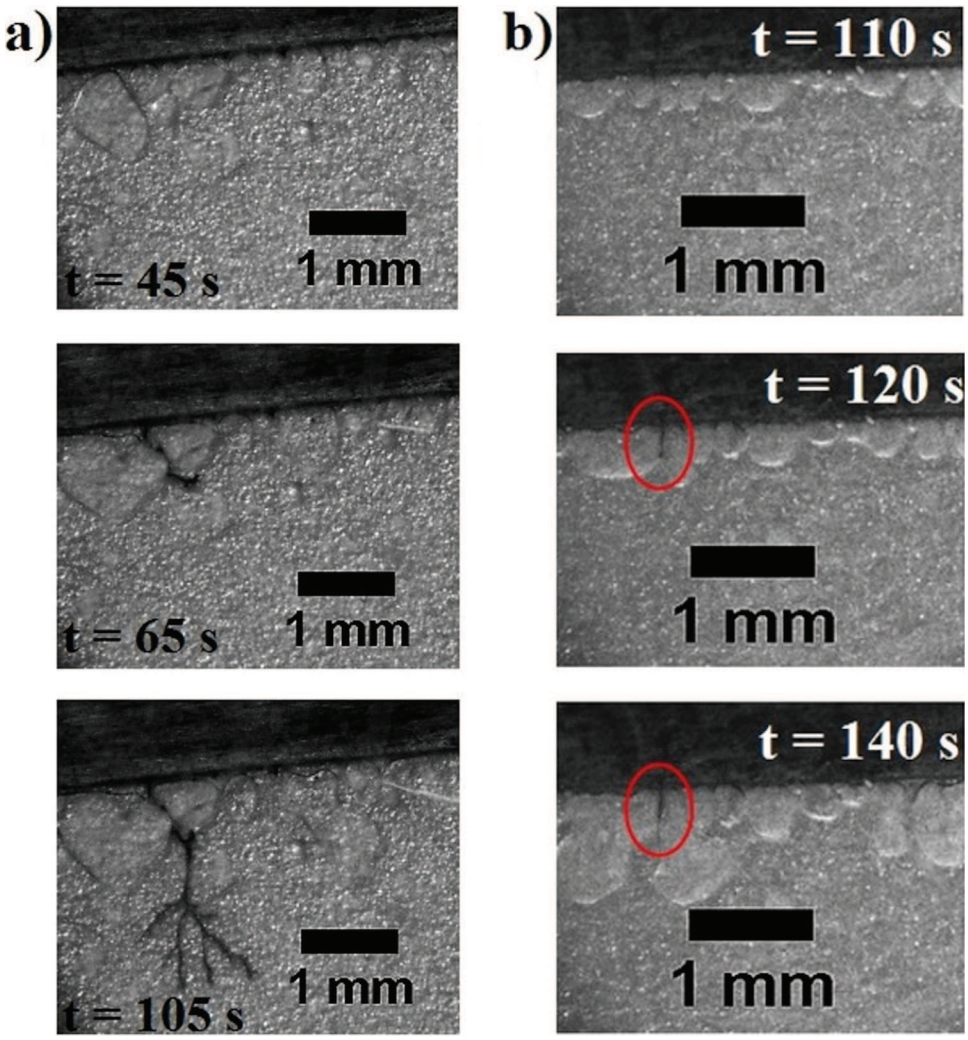


**Fig. 4.** Optical images taken during galvanostatic electrolyses in the Hele-Shaw cell for a) 0.02 M $FeCl_2$, $j = 12\ mA/cm^2$ and b) 0.1 M $FeCl_2$, $j = 16\ mA/cm^2$. With these values of applied current density, the $H_2$ bubbles progressively block the electrode surface, that could favor the start of the growth of a branch a) but also its stop b) (see the branch in the red circle). (For interpretation of the references to colour in this figure legend, the reader is referred to the web version of this article.)

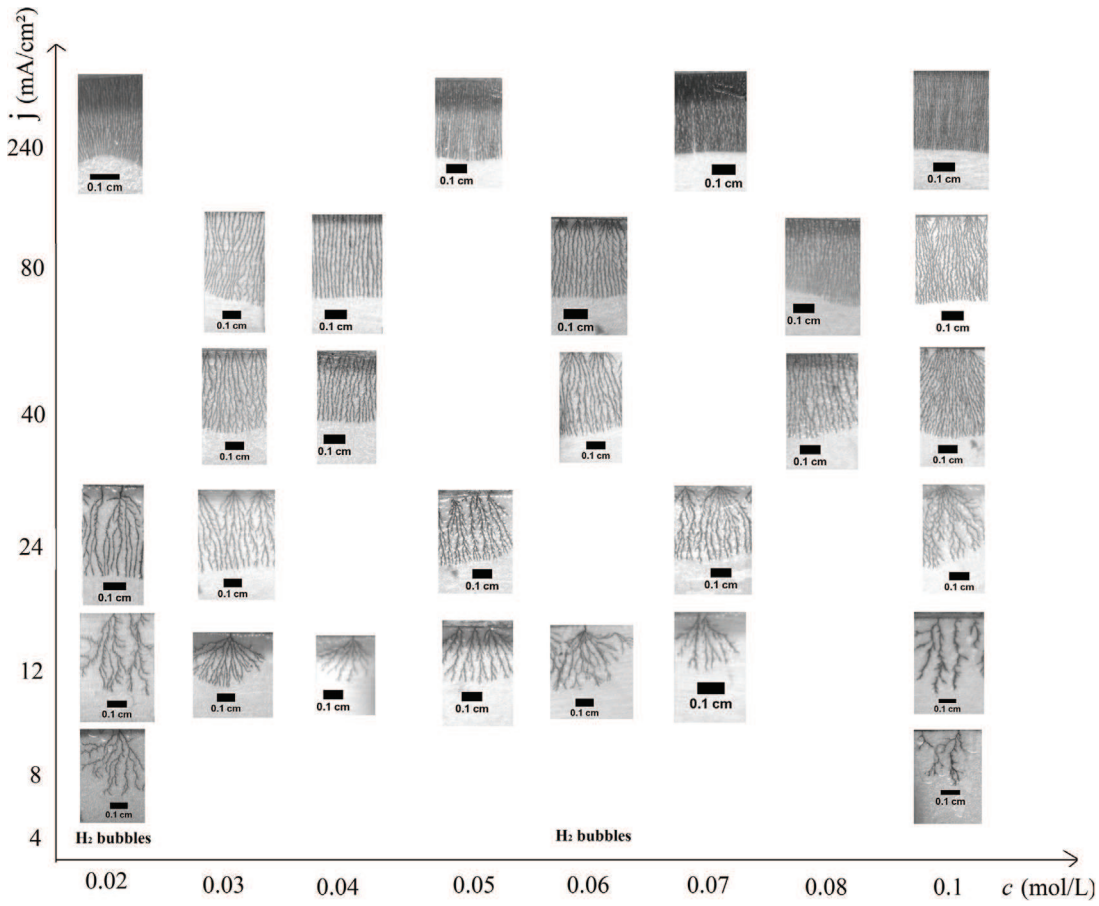


**Fig. 5.** Optical images of the different deposit morphologies obtained using the Hele-Shaw cell for the galvanostatic electrolyses: $8 \leq j \leq 240$ mA/cm$^2$ and $0.02 \leq FeCl_2 \leq 0.1$ M.

branches, has been confirmed by magnified visualizations for all the deposits.

The columnar morphology, which consists of a large number of branches regularly spaced and growing at the same velocity, is obtained mainly for the current densities higher than 24 mA/cm$^2$, whatever the precursor concentration. Increasing the current density causes the distance between the branches to decrease which leads to apparently denser deposits.

Lower current densities, typically a value of 12 mA/cm$^2$, produce deposits with fractal-like morphology, which exhibit open structures with fewer branches, and their arrangement is also less regular than the one obtained for columnar deposits.

Such a transition, from the fractal to the columnar morphologies when the polarization magnitude is increased, has often been reported for the electrochemical growth of ramified metals without $H_2$ bubbles co-formation (zinc [18,31] copper [30–33]), however the mechanism of this transition is not yet fully understood.

One convincing explanation is the relatively low electrical conductivity of the porous branches which regulates the heights of the branches and thus stabilizes the growth front, especially at high applied current densities [34]. Note that electroconvective phenomena have also been proposed to explain this transition [33].

The dendritic morphology corresponds to an ordered crystal growth (of few main trunks with secondary branches tilted with a well-defined angle); it is obtained when the growth of metallic crystals is favored comparatively to nucleation events, generally at the highest applied currents (the deposit morphology goes from fractal to columnar and then to dendritic when the applied current increases) [18]. In the present study (Fig. 5) no dendrites are observed at the macroscopic scale, the columnar morphology predominates even at high applied currents. However, as it is shown in the next section (Fig. 7), the morphology is actually dendritic at a smaller length scale. It means that there is still a competition between nucleation and growth events when the applied current is high; the dendrites growth is regularly and early stopped by nucleation events. This could be due to the co-produced $H_2$ bubbles around the iron branches which act as "insulating shields" that limit the lateral growth of secondary branches of the dendrites and ensure a constant separation distance between the branches.

To sum up, the co-formation of $H_2$ bubbles does not affect significantly the transition between the main patterns usually observed for other systems in absence of $H_2$ bubbles. The bubbles can only be suspected of affecting the transition between the columnar and the dendritic morphologies by a lateral shielding effect which limits the dendrites growth at high applied currents.

### 3.3. Faradaic yield of the iron electrodeposition

As indicated in the section 3.1, the deposit growth appears to be less affected by the co-production of $H_2$ bubbles at high current density, and so for columnar deposits (section 3.2). For this particular case, the faradaic yield of the iron electrodeposition process is estimated from the measurement of the growth front velocity and the theory developed in [16].

When metallic branches grow without the formation of $H_2$ bubbles (case of copper or zinc), during galvanostatic electrolyses, the corresponding columnar deposits are bounded by a flat front

which advances at a constant and predictable velocity $v_g$ [16]. The concentration profile of the electroactive species, ahead of the growth front, is then stationary and it is advected with the front. Without supporting electrolyte, the mass transfer problem can be reduced to a generic diffusion-advection problem ([35]) that has been used in [16] to obtain the following modeling of the concentration profile $c(x,t)$ ahead of the front:

$$\frac{c(x,t)}{c^{\infty}} = 1 - \exp\left(\frac{x_f(t) - x}{Ld}\right), \tag{8}$$

with $c^{\infty}$ the bulk concentration, $x_f(t)$ the growth front location, $x$ the coordinate perpendicular to the front and directed towards the growth direction and $Ld = \overline{D}/v_g$ the diffusion length, $\overline{D} = \frac{z^+u^+D^+ - z^-u^-D^-}{z^+u^+ - z^-u^-}$ being the diffusion coefficient of the unsupported electrolyte (where $z^+$, $z^-$and $u^+$, $u^-$ are the valences and the mobilities of the cationic and anionic species of the electrolyte respectively) [35].

Combining Equation (8) with the boundary condition at the front for the current density (assuming that the metal electrodeposition is quantitative) $\frac{j}{z^+F} = \frac{\overline{D}}{1-t^+}\frac{\partial c}{\partial x}|_{xf}$ (where $\frac{\partial c}{\partial x}|_{xf} = \frac{c^{\infty}}{Ld}$, $t^+ = \frac{z^+u^+}{z^+u^+ - z^-u^-}$ is the transference number and $F$ is the Faraday's constant) [35], the growth velocity of the columnar deposits (without $H_2$ bubbles formation) is given by [16]:

$$v_g = \frac{j(1-t^+)}{z^+Fc^{\infty}} \tag{9}$$

In Fig. 6, for several columnar iron deposits produced in the present study, the measured growth front velocity $v_{exp}$ is plotted as a function of the ratio $\frac{j}{2Fc^{\infty}}$, assuming a faradaic yield of 100% ($j$ is the current applied). As predicted, $v_{exp}$ depends linearly on $\frac{j}{2Fc^{\infty}}$ and the proportionality factor is equal to 0.56. Thus the $t^+$ value determined via this experimental approach, assuming a faradaic yield of 100%, is 0.44. By comparing this experimental $t^+$ value to the theoretical one ($t^+ = \frac{z^+u^+}{z^+u^+ - z^-u^-}$), the actual faradaic yield of the iron electrodeposition can be estimated.

According to [36], for chloride ions concentration lower than 1 mol/kg, $Fe^{2+}$ ions are not complexed with the chloride ions. Therefore here, it is assumed that $FeCl_2$ is fully dissociated into $Fe^{2+}$ and $Cl^-$ without the formation of complexes. The $H^+$ concentration being always well lower than $Fe^{2+}$ or $Cl^-$ concentrations, the main

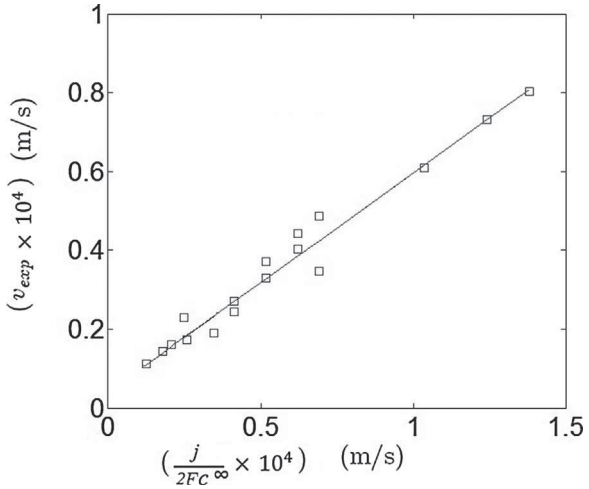


**Fig. 6.** Average growth velocity of columnar deposits as a function of the ratio $\frac{j}{2Fc^{\infty}}$. Squares: experimental data; line: best linear fit, $v_{exp} = 0.56 \times \left(\frac{j}{2Fc^{\infty}}\right) + 4.3 \times 10^{-6}$; concentrations range from 0.02 to 0.1 M and current densities from 24 to 240 mA/cm$^2$.

cations and anions to consider for the determination of the theoretical $t^+$ value are the $Fe^{2+}$ and the $Cl^-$ ions. A theoretical $t^+$ value of 0.41 is determined (assuming an infinite dilution of the species, $u^{\pm} = D^{\pm}/RT$, $R = 8.314$ J/(mol·K), $T = 293$ K, $D^+ = 7.19 \times 10^{-10}$ m$^2$/s [37] and $D^- = 2.03 \times 10^{-9}$ m$^2$/s [38]) which is slightly lower than the $t^+$ value determined with the experimental data (Fig. 6): 0.44. This difference between experimental data and theory can be interpreted as a consequence of the $H^+$ co-reduction. Indeed, the whole current density is not used to the iron electrodeposition and thus, in the experiments carried out, the deposit front advances a little more slowly than expected by the theory, assuming a faradaic yield of 100%. Therefore, the actual faradaic yield for the electrodeposition of the columnar deposits is estimated at 95%.

These results show that, during the electrodeposition of columnar deposits, an almost negligible part (5%) of the applied current density $j$ is allotted to the $H^+$ reduction. Nevertheless, even if little $H_2$ gas is generated, the bubbles are well visible since they are highly crushed in the very thin Hele-Shaw cell used.

### 3.4. Small-scale structure of the ramified iron branches

With the objective of using the microstructure of the ramified deposits, to produce a suspension of iron nanoparticles, the small scale structure of the iron branches, obtained in the Hele-Shaw cell, is observed by SEM.

Among the various deposits obtained in this study, five deposits, showing morphologies going from columnar to fractal ($8 \le j \le 24$ mA/cm$^2$), have been observed by SEM and the pictures are presented in Fig. 7: the deposits shown in Fig. 7a), b) and c) are obtained using a 0.02 M $FeCl_2$ solution at current densities of 24, 12 and 8 mA/cm$^2$ respectively; the deposits shown in Fig. 7d) and e) are obtained using a 0.1 M $FeCl_2$ solution at current densities of 12 and 8 mA/cm$^2$ respectively. To compare the large and the small scale structures simultaneously, three different magnifications are provided in Fig. 7.

For the deposits obtained with a concentration of 0.02 M and at current densities ranging from 24 to 8 mA/cm$^2$ (Fig. 7a), b) and c)) the small scale structure (pictures in the middle) reveals dendritic-like branches (main trunks with secondary branches highlighting preferred growth orientation) which consist, however, at the nanometric scale (zoom on the right), of small crystallites. The size of these crystallites varies from one deposit to another. The deposit shown in Fig. 7a) (24 mA/cm$^2$, 0.02 M) appears to consist of several rows of regular crystallites, with a size of about 20 nm, while for the deposit shown in Fig. 7b) (12 mA/cm$^2$, 0.02 M), the crystallites size lies in the range of 50–100 nm.

Fleury correlates this fine granular structure to the oscillatory character of the nucleation kinetics and claims that the crystallites size is dictated by the growth velocity, and so by the current density (for the ramified growth of copper [19]): the higher the growth velocity, the smaller the crystallites are.

Regarding comparatively the apparent growth velocity and the crystallites size $v_{(24\text{mA/cm}^2,\ 0.02\text{M})} \approx 40\ \mu\text{m/s} \rightarrow 10 \le d_{\text{crystallites}}(\text{nm}) \le 30$; $v_{(12\text{mA/cm}^2,\ 0.02\text{M})} \approx 20\ \mu\text{m/s} \rightarrow 50 \le d_{\text{crystallites}}(\text{nm}) \le 100$) it can be concluded that these observations, for the iron case, are consistent with the affirmation of Fleury ([19]).

In addition, our results highlight that the influence of the growth velocity on the crystallites size has a direct impact on the regularity of the deposit structure. The fractal deposit obtained with 8 mA/cm$^2$ (0.02 M), Fig. 7c), shows a small scale structure (picture in the middle) less regular than the deposits obtained with higher current densities, 24 and 12 mA/cm$^2$ (0.02 M), Fig. 7a) and b). This deposit exhibits, at the nanometric scale (picture on the right) big crystallites of various sizes ranging between 200 and

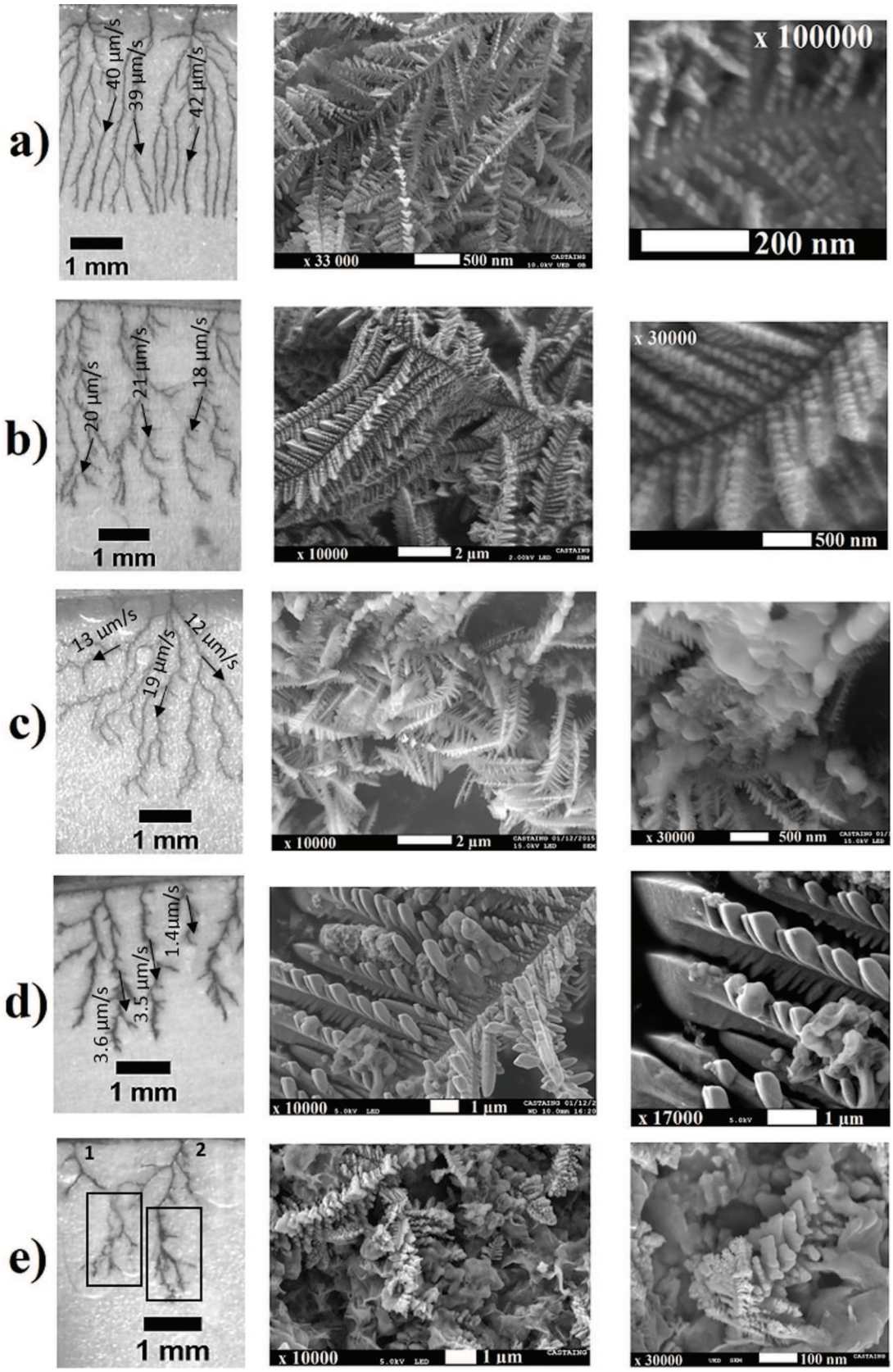


**Fig. 7.** SEM pictures of iron electrodeposits obtained in the Hele-Shaw cell at various current densities and using various precursor concentrations. a), b), c) 0.02 M $FeCl_2$ using 24, 12 and 8 mA/cm$^2$ respectively; d), e): 0.1 M $FeCl_2$ using 12 and 8 mA/cm$^2$ respectively. Millimetric (left column), micrometric (middle column) and nanometric (right column) scales. Some values of the growth velocity are indicated on the left pictures.

500 nm. This broad range of crystallites size, in the same deposit, is explained by the fractal morphology. Indeed, contrary to the columnar deposit, for a fractal deposit, the growth velocity is not the same for all the branches, the growth of some branches can slow down and stop in favor of the growth of others. The estimation of the growth velocity of some branches leads to values varying from 12 μm/s to 19 μm/s (Fig. 7c) on the left) which explains the dispersion of crystallites sizes observed.

The deposits shown in Fig. 7d) and e) are obtained using a higher concentration of 0.1 M, at two current densities, 12 and 8 mA/cm$^2$ respectively. At the large scale (pictures on the left), the deposit obtained at 12 mA/cm$^2$ (Fig. 7d)), shows thicker branches than the other deposits. At the small scale, the structure is ordered and the size of the crystallites, composing the branches, ranges between 500 nm and 1 μm (pictures in the middle and on the right). This is consistent with the low growth velocity estimated for most of the branches of this deposit ≈ 3.6 μm/s; this last value is about four times slower than the velocity value measured in the previous cases.

Finally, the deposit obtained at 8 mA/cm$^2$ (Fig. 7e)) shows, at the large scale, fractal morphology, but it can be noticed that large $H_2$ bubbles have been formed during its growth. Regarding the SEM pictures (Picture in the middle), it can be observed that the deposit shows a really complex small-scale structure. A wide variety of structures is observed (thin branches, rough structures, smooth iron blocks...), probably because the generation of $H_2$ bubbles disturbes strongly the deposit growth. For example, the growth of the branch labeled "1" in Fig. 7e), has been stopped by the presence of an $H_2$ bubble. Considering the branch labeled "2" in Fig. 7e), the observations made during the electrolysis, show that the growth of the right branch is stopped for the benefit of the left branch. Then, the left branch growth is stopped by the presence of a bubble, which reactivates the growth of the right branch. Thus, the growth of one branch is achieved in several steps with different growth velocities.

To sum up, the SEM observations have confirmed the Fleury's work [19] for the iron case: the iron branches consist of crystallites whose size decreases with increasing their growth velocity. In addition, the regularity of the crystallites size, observed at the nanometric scale, is related to the large-scale morphology of the deposits. Fractal deposits consist of polydispersed crystallites while columnar deposits show crystallites of almost uniform size. The deposits homogeneity is even more affected when $H_2$ bubbles hinder the deposit growth.

In conclusion, in the prospect of the fragmentation of the iron branches to produce regular iron nanoparticles, the operating conditions allowing the growth of columnar deposits should be favored.

### 3.5. Characterization of the produced particles after fragmentation

After the formation of a columnar deposit (80 mA/cm$^2$, 0.1 M of $FeCl_2$) and its rinsing, the PZT is activated (square electrical signal: peak to peak voltage = 250 V, frequency = 4 kHz, duration = 15 s). The characterization by TEM of the collected particles (Fig. 8) reveals that they are in fact fragmented dendrites of various sizes, from few micrometers (Fig. 8a), b) and c)) to hundreds of nanometers (Fig. 8e) and f)). These fragments of dendrites, shown in Fig. 8a), b) and c), were probably initially secondary branches of main trunks which have been cut off at their root. In Fig. 8a) and b), the micrometric fragments seem to be unaffected by the fragmentation process, while in Fig. 8c) the fragment seems to have been peeled off on its right side. This suggests that smaller fragments (∼200 nm) are broken by the mechanical stress induced by bubbles oscillations. A pile of dendrites along with a group of smaller entities can be seen in Fig. 8d). They consist of needle-like fragments which appear to be the small branches of the secondary branches.

It can be concluded, that coupling the electrochemical formation of ramified iron branches with their fragmentation, using the elaborated "Electrochemical and Vibrating Hele-Shaw cell", enables to obtain a suspension of dendritic particles of sizes varying from hundreds of nanometers to few micrometers. However, the main interest of using nanoparticles is their high specific surface, and even if the obtained fragments are about 1 μm, their dendritic shape gives them a high surface to volume

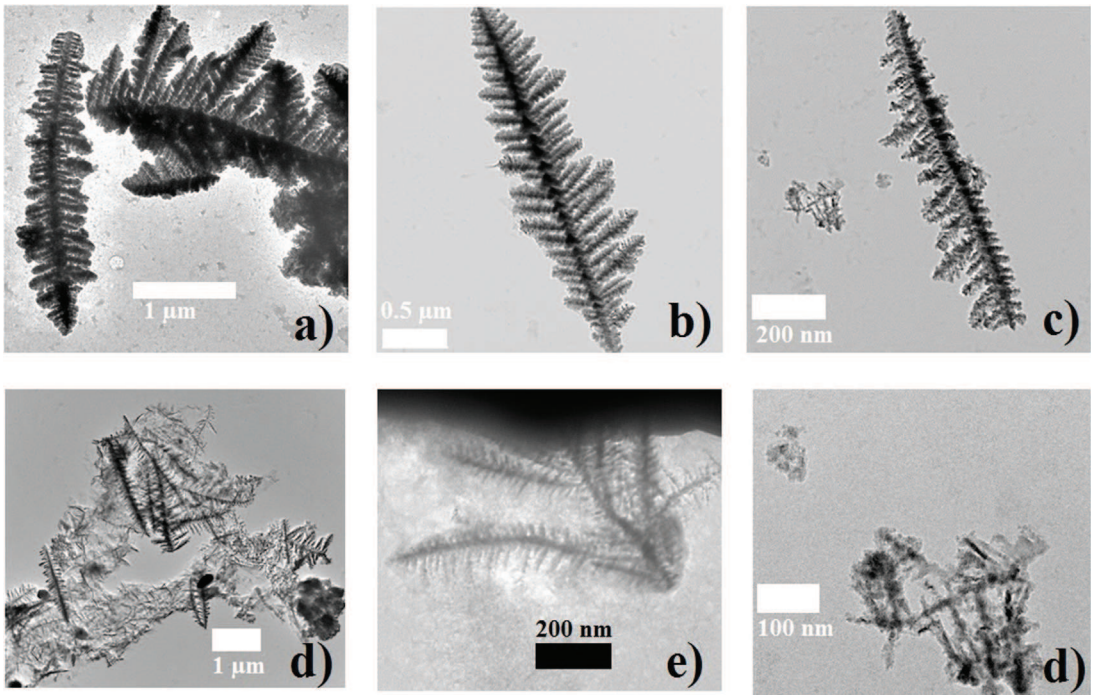


**Fig. 8.** TEM pictures of fragments of iron dendrites obtained after the fragmentation of the columnar deposit ($j$ = 80 mA/cm$^2$, 0.1 M $FeCl_2$) by acoustic vibrations of the PZT.

ratio. Thanks to an image processing, a perimeter to surface ratio of $1.3 \times 10^8\ m^{-1}$ has been determined, which corresponds to a nanoparticle of about 30 nm in diameter. Therefore, these fragments should show a high catalytic activity that will be studied shortly.

### 3.6. Purity of the produced suspension

The particles of interest being initially the building elements of the iron branches, they are, at first, immobilized inside the Hele-Shaw cell (in the branches). This offers the possibility to rinse the particles (before the deposit fragmentation) by a simple flow of deaerated water in order to decrease the concentration of the remaining electrolyte (used for the iron deposit production) in the cell. Consequently, contrary to other syntheses, the produced suspension is purified in-situ and therefore no additional purification step should be required.

However, since the electrolyte cannot be totally removed, its residual concentration is measured, here for a particular case (columnar deposit, formed using a current density of 80 mA/cm$^2$ and 0.1 M of $FeCl_2$), and the purity of the produced suspension (defined here as the mass fraction of metallic iron excluding the solvent $H_2O$), is also estimated.

After the formation of the deposit, 1 mL of deaerated ultrapure water (∼90 times the volume of the Hele-Shaw cell) is injected into the cell at a flow rate of ∼100 μL/min (∼10 min). After the fragmentation, ∼700 μL of the produced suspension is collected by a flow of deaerated ultrapure water. The mass concentration of the remaining $Fe^{2+}$ and $Cl^-$ in this volume is respectively $\sim 1.11 \times 10^{-2}$ g/L and $\sim 1.42 \times 10^{-2}$ g/L (titration of chloride ions by $AgNO_3$). The mass concentration of metallic iron is equal to $1.23 \times 10^{-1}$ g/L (estimated by the passed charge during the electrolysis and assuming that all the particles are collected). Therefore, the purity of the produced suspension is high and equal to 83%. This value of purity obtained is now compared to the one reached with the colloidal and the sonoelectrochemical syntheses.

In the colloidal synthesis of iron nanoparticles, the commonly employed concentration of both the metal precursor and the reducing agent is in the range $1–10^{-2}$ M [12,39] that leads, at the end of the synthesis, to the same range of byproducts concentration (NaCl, $B(OH)_3$ . . . ). Considering the typical synthesis reaction [11,40]:

$$FeCl_3 + 3NaBH_4 + 9H_2O \rightarrow Fe^0 + 3NaCl + 3B(OH)_3 + 10.5H_2, \quad (10)$$

and, assuming a stoichiometric initial composition and a total reaction, the purity of the produced suspension could be estimated: 13%.

In the sonoelectrochemical synthesis, the use of supporting electrolyte in a concentration range ∼0.5 M prevents reaching high purity values. In fact, for this synthesis way, the purity depends on both the experimental configuration (especially the ratio between the surface of the electrode and the volume of the reactor) and the production duration.

Therefore, in the proposed synthesis, even if the electrolyte was not totally removed during the rinsing phase, the purity of the produced suspension is well higher than in the colloidal and sonoelectrochemical syntheses. Even higher purity and concentration of iron particles can be achieved by optimizing the outlet of the device using smaller and shorter tubes.

## 4. Conclusions

The objective of this work is to explore a new synthesis route for the production of iron nanoparticles using a simple aqueous ferrous solution ($FeCl_2$) in an electrochemical and vibrating Hele-Shaw cell. The use of this confined cell (50 μm deep), allows the growth of ramified branches with a granular microstructure. The growth of the branches is accompanied by the formation of $H_2$ bubbles which, due to their oscillations during the vibration phase (activation of the PZT), allow fragmenting the branches. The influence of the operating conditions (applied current density and $FeCl_2$ concentration) on the electrodeposition is studied. The focus is on the growth of $H_2$ bubbles and on the obtained branches pattern and microstructure. Columnar deposits (ensuring regular branches growth), with embedded $H_2$ bubbles (only 5% of the applied current is used for their generation), are obtained for sufficiently high applied current densities (>∼24 mA/cm$^2$). SEM images of the branches reveal a dendritic structure consisting of crystallites of almost uniform size. This size depends on the local branch growth velocity. Increasing this growth velocity from ∼20 μm/s to ∼40 μm/s causes the average diameter of the crystallites to decrease from the range of 50–100 nm to 10–30 nm. TEM images of the particles, obtained after activation of the PZT, have revealed that their sizes range from hundreds of nanometers to few micrometers. So, this process has not allowed producing monodispersed nanoparticles. However, the proposed synthesis way has the following advantages:

- the produced submicrometric iron dendrites have a high specific surface (perimeter to surface ratio of $1.3 \times 10^8\ m^{-1}$ comparable to a nanoparticle of 30 nm diameter), they are consequently well suited for catalysis applications
- the purity of the produced suspension is well higher (∼83%) than the one obtained with other wet-chemical synthesis ways (colloidal and sonoelectrochemical), the purification step could be suppressed if it is not required in the application
- the initial solution contains only a cheap ferrous salt

Consequently, this synthesis way could be used for cost effective and rapid production of “ready to use” iron particles mainly for catalysis purposes.

This work is the first step for the development of a new synthesis way, the device and the method could be optimized on several points. Concerning the electrodeposition phase, it is well known that the morphology of the deposited metal depends on the counter-ion and on the presence of additives (surfactants, polymers, chlorides, nitrates, . . . ) and thus the structure of the particles could be tuned by the solution composition. This could lead to the production of tailored particles as well as to easier to fragment deposits. Concerning the fragmentation phase, here, the oscillations of the naturally co-produced $H_2$ bubbles, induced by the vibrations of the PZT, are exploited. Microfluidic-like strategies could be employed to control precisely the location of oscillating bubbles inside the channel to improve the efficiency of the fragmentation phase and thus reach even smaller particles. Finally, this synthesis could be extended to other metals, the only prerequisite being that the metal has to be able to form ramified branches.

## Acknowledgements

The authors are very grateful to M. L. de Solan-Bethmale (Laboratoire de Génie Chimique), S. Le Blond du Plouy and L. Weingarten (Centre de microcaractérisation Raimond Castaing) for SEM and TEM observations.

## References

[1] Y.J. Wang, S.M. Hussain, G.P. Krestin, Superparamagnetic iron oxide contrast agents: Physicochemical characteristics and applications in MR imaging, Eur. Radiol. 11 (2001) 2319–2331.

[2] A. Jordan, R. Scholz, P. Wust, H. Fähling, R. Felix, Magnetic fluid hyperthermia (MFH): Cancer treatment with AC magnetic field induced excitation of biocompatible superparamagnetic nanoparticles, J. Magn. Magn. Mater. 201 (1999) 413–419.
[3] C.G. Hadjipanayis, M.J. Bonder, S. Balakrishnan, X. Wang, H. Mao, G.C. Hadjipanayis, Metallic iron nanoparticles for MRI contrast enhancement and local hyperthermia, Small. 4 (2008) 1925–1929.
[4] R.A. Crane, T.B. Scott, Nanoscale zero-valent iron: Future prospects for an emerging water treatment technology, J. Hazard. Mater. 211–212 (2012) 112–125.
[5] X. Li, D.W. Elliott, W. Zhang, Zero-Valent iron nanoparticles for abatement of environmental pollutants: Materials and engineering aspects, Crit. Rev. Solid State Mater. Sci. 31 (2006) 111–122.
[6] D.L. Huber, Synthesis, properties, and applications of iron nanoparticles, Small 1 (2005) 482–501.
[7] W. Yan, H.L. Lien, B.E. Koel, W. Zhang, Iron nanoparticles for environmental clean-up: recent developments and future outlook, Environ. Sci. Process. Impacts 15 (2013) 63.
[8] J.E. Muñoz, J. Cervantes, R. Esparza, G. Rosas, Iron nanoparticles produced by high-energy ball milling, J. Nanoparticle Res. 9 (2007) 945–950.
[9] L.B. Hoch, E.J. Mack, B.W. Hydutsky, J.M. Hershman, J.M. Skluzacek, T.E. Mallouk, Carbothermal synthesis of carbon-supported nanoscale zero-valent iron particles for the remediation of hexavalent chromium, Environ. Sci. Technol. 42 (2008) 2600–2605.
[10] M. Bystrzejewski, Synthesis of carbon-encapsulated iron nanoparticles via solid state reduction of iron oxide nanoparticles, J. Solid State Chem. 184 (2011) 1492–1498.
[11] C. Wang, W. Zhang, Synthesizing nanoscale iron particles for rapid and complete dechlorination of TCE and PCBs, Environ. Sci. Technol. 31 (1997) 2154–2156.
[12] F. He, D. Zhao, Manipulating the size and dispersibility of zerovalent iron nanoparticles by use of carboxymethyl cellulose stabilizers, Environ. Sci. Technol. 41 (2007) 6216–6221.
[13] T. Wang, X. Jin, Z. Chen, M. Megharaj, R. Naidu, Green synthesis of Fe nanoparticles using eucalyptus leaf extracts for treatment of eutrophic wastewater, Sci. Total Environ. 466-467 (2014) 210–213.
[14] A. Khachatryan, R. Sarkissyan, L. Hassratyan, V. Khachatryan, Influence of ultrasound on nanostructural iron formed by electrochemical reduction, Ultrason. Sonochem. 11 (2004) 405–408.
[15] V. Zin, B.G. Pollet, M. Dabalà, Sonoelectrochemical (20 kHz) production of platinum nanoparticles from aqueous solutions, Electrochim. Acta 54 (2009) 7201–7206.
[16] C. Léger, J. Elezgaray, F. Argoul, Internal structure of dense electrodeposits, Phys. Rev. E – Stat. Physics Plasmas, Fluids, Relat. Interdiscip. Top. 61 (2000) 5452–5463.
[17] Y. Sawada, A. Dougherty, J.P. Gollub, Dendritic and fractal patterns in electrolytic metal deposits, Phys. Rev. Lett. 56 (1986) 1260–1263.
[18] D. Grier, E. Ben-Jacob, R. Clarke, L.M. Sander, Morphology and microstructure in electrochemical deposition of zinc, Phys. Rev. Lett. 56 (1986) 1264–1267.
[19] V. Fleury, Branched fractal patterns in non-equilibrium electrochemical deposition from oscillatory nucleation and growth, Nature 390 (1997) 145–148.
[20] A. Iranzo, F. Chauvet, T. Tzedakis, Influence of electrode material and roughness on iron electrodeposits dispersion by ultrasonification, Electrochim. Acta 184 (2015) 436–451.
[21] D. Grujicic, B. Pesic, Iron nucleation mechanisms on vitreous carbon during electrodeposition from sulfate and chloride solutions, Electrochim. Acta 50 (2005) 4405–4418.
[22] S. Bodea, L. Vignon, R. Ballou, P. Molho, L.L. Néel, G. Cedex, Electrochemical Growth of Iron Arborescences under In-Plane Magnetic Field: Morphology Symmetry Breaking, Phys. Rev. Lett. 83 (1999) 2612–2615.
[23] R.H. Liu, J. Yang, M.Z. Pindera, M. Athavale, P. Grodzinski, Bubble-induced acoustic micromixing, Lab Chip. 2 (2002) 151–157.
[24] S.S. Wang, Z.J. Jiao, X.Y. Huang, C. Yang, N.T. Nguyen, Acoustically induced bubbles in a microfluidic channel for mixing enhancement, Microfluid. Nanofluidics 6 (2009) 847–852.
[25] D. Ahmed, X. Mao, J. Shi, B.K. Juluri, T.J. Huang, A millisecond micromixer via single-bubble-based acoustic streaming, Lab Chip. 9 (2009) 2738–2741.
[26] W.L. Nyborg, Acoustic streaming, in: W.P. Mason (Ed.), Physical acoustics, Vol. 2B, Academic Press, New York, 1965.
[27] K. Nishikawa, Y. Fukunaka, E. Chassaing, M. Rosso, Electrodeposition of metals in microgravity conditions, Electrochim Acta 1 (2013) 15–21.
[28] G. Marshall, E. Mocskos, G. González, S. Dengra, F.V. Molina, C. Iemmi, Stable, quasi-stable and unstable physicochemical hydrodynamic flows in thin-layer cell electrodeposition, Electrochim. Acta. 51 (2006) 3058–3065.
[29] V. Heresanu, Electrodéposition sous champ magétique de zinc et de fer. Propriétés magnétiques des arborescences de fer, Ph.D. thesis, Université Joseph Fourier, Grenoble, 2003, pp. 1.
[30] C. Léger, L'électrodéposition en cellule mince sous l'oeil d'un interférometre: une étude expérimentale et théorique de processus limités par la diffusion, Ph. D thesis, Université de Bordeaux I, 1999.
[31] J.M. Huth, H.L. Swinney, W.D. McCormick, A. Kuhn, F. Argoul, Role of convection in thin-layer electrodeposition, Phys. Rev. E. 51 (1995) 3444–3458.
[32] I.B. Hibbert, J.R. Melrose, Copper electrodeposits in paper support, Phys. Rev. A 38 (1987) 1036–1048.
[33] V. Fleury, J.H. Kaufman, D.B. Hibbert, Mechanism of a morphology transiion in ramified electrochemical growth, Nature 367 (1994) 435–438.
[34] J.K. Lin, D.G. Grier, Stability of densely branched growth in dissipative diffusion-controlled systems, Phys. Rev. E 54 (1996) 2690–2695.
[35] J. Newman, K.E. Thomas-Alyea, Electrochemical Systems, Third Edition, John Wiley & Sons, 2004.
[36] R.H. Zhao, P.J. Pan, A spectrophotometric study of Fe(II)-Chloride complexes in aqueous solutions from 10 to 100 °C, Can. J. Chem. Can. Chim. 79 (2001) 131–144.
[37] Y. Li, S. Gregory, Diffusion of ions in sea water and in deep sea sediments, Geochim. Cosmochim. Acta 38 (1973) (1974) 703–714.
[38] E. Samson, J. Marchand, K.A. Snyder, Calculation of ionic diffusion coefficients on the basis of migration test results, Mater. Struct. Constr. 36 (2003) 156–165.
[39] Y. Liu, S.A. Majetich, D.S. Sholl, G.V. Lowry, TCE Dechlorination Rates Pathways, and Efficiency of Nanoscale Iron Particles with Different Properties, Environ. Sci. Technol. 39 (2005) 1338–1345.
[40] G. Zhang, Y. Liao, I. Baker, Surface engineering of core/shell iron/iron oxide nanoparticles from microemulsions for hyperthermia, Mater. Sci. Eng. C. 30 (2010) 92–97.